

An upgraded focal plane detector for the MAGNEX spectrometer

D. Torresi^{a,*}, O. Sgouros^a, V. Soukeras^a, M. Cavallaro^a, F. Cappuzzello^{a,b}, D. Carbone^a, C. Agodi^a, G. A. Brischetto^{a,b,c}, S. Calabrese^{a,b}, I. Ciraldo^{a,b}, N. Deshmukh^{a,1}, A. Hacisalihoglu^{a,d}, L. La Fauci^{a,b}, A. Spatafora^{a,b}, for the NUMEN collaboration

^a*INFN - Laboratori Nazionali del Sud, Catania, Italy*

^b*Dipartimento di fisica e astronomia - Università di Catania, Catania, Italy*

^c*Centro Siciliano di Fisica Nucleare e Struttura della Materia (CSFNSM), Catania, Italy*

^d*Akdeniz University, Antalya, Turkey*

Abstract

An upgraded and improved version of the focal plane detector (FPD) of the large-acceptance magnetic spectrometer MAGNEX is described here. The FPD consists of a tracker operating at low pressure and of a silicon detector wall. Thanks to a different geometry of the electron multiplication and induction elements, the new detector guarantees a superior signal to noise ratio, resulting in a more accurate tracking and a cleaner identification of the detected heavy ions. The new detector has been tested by using a ^{18}O beam at an energy of 84 MeV. A description of the new FPD that pinpoints the innovation and the obtained performances is given and discussed in details.

Keywords: Magnetic spectrometer, Focal plane detector, MAGNEX

1. Introduction

Modern nuclear physics studies often require to join the advantages of the magnetic spectrometry (strong rejection factors of reaction products, zero-degree measurements, etc.) with the possibility to measure heavy ions.

*Corresponding author

Email address: domenico.torresi@lns.infn.it (D. Torresi)

¹present address: Nuclear Physics Division, Saha Institute of Nuclear Physics, Kolkata, West Bengal 700064, India

Moreover, in order to explore rare nuclear processes [1, 2, 3], modern magnetic spectrometers have grown toward large acceptance in momentum and solid angle as well as large dynamic range in mass and energy [4, 5, 6, 7]. An example of this class of devices is the MAGNEX spectrometer [8, 9, 10] installed at the INFN-LNS laboratory in Catania. Its magnetic structure, based on a vertically focusing quadrupole and a horizontally dispersing and focusing bending magnet, ensures a momentum acceptance of about 24% and a solid angle of 50 msr. The development of large-acceptance magnetic spectrometers requires more advanced Focal Plane Detectors (FPD). These have to provide not only an unambiguous particle identification, but also an accurate three-dimensional tracking of the ions trajectory downstream of the magnetic elements [11, 12, 13, 14]. The FPDs are, therefore, the heart of the modern large-acceptance magnetic spectrometers. In the present paper the upgrade of MAGNEX FPD [15] will be described. The new FPD has been developed with the aim to improve the tracking and the identification performances.

The paper is organized as follows: Section 2 describes the design of the new detector, emphasizing the new adopted solutions compared to the previous ones; Section 3 presents a detailed characterization of the new FPD response to beam generated ions; Section 4 summarizes the results and our conclusions.

2. Focal plane detector design

The MAGNEX FPD consists of two sections: a gas tracker sensitive to the energy loss of the ions and a stopping wall for the measurements of their residual energy [15]. The gas tracker is a proportional drift chamber with a total active volume of $1360 \times 200 \times 90$ mm³, divided in six sections that are six independent position-sensitive proportional counters, whereas the stopping wall, placed behind the gas tracker, is made of 57 silicon pad detectors covering an area of 1360×200 mm², see Fig. 1.

2.1. The gas tracker

The gas tracker is contained in a vacuum chamber that is isolated from the high-vacuum upstream region by a large mylar[®] window (220×920 mm²) with typical thickness ranging from 1.5 to 6 μ m, depending on the pressure filling the chamber. The active region is filled with 99.95% isobutane at pressure that ranges from few mbar up to several tenths of mbar. The use

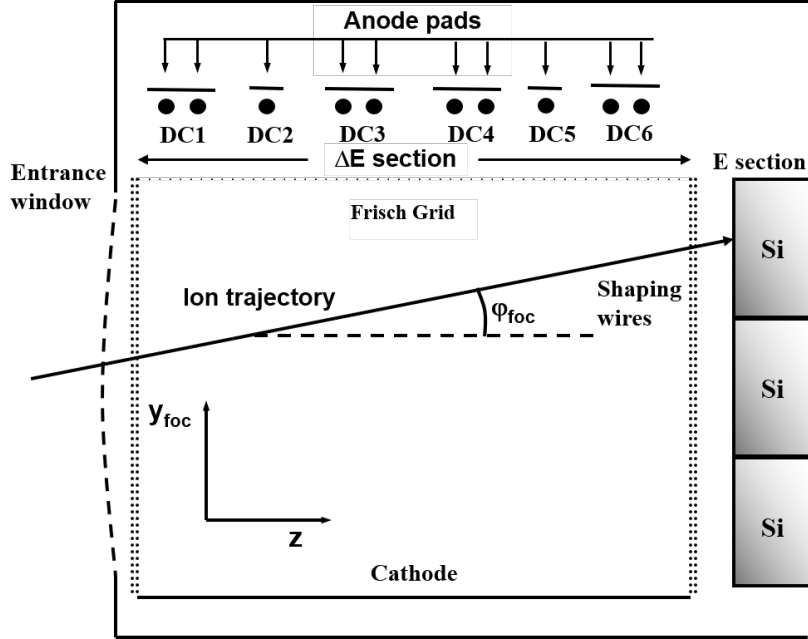


Figure 1: Sketch of the lateral view of the new MAGNEX FPD.

of pure isobutane guarantees a fast drift velocity and very good operational stability, [16, 17, 18]. In order to avoid further dead layer there is no exit window, the silicon detectors of the stopping wall are therefore embedded in the gas. The FPD vacuum chamber is movable of ± 0.08 m along the optical axis of the spectrometer to allow to translate the focal plane according to different focus conditions. In order to reduce the effect of the chromatic aberrations the FPD is tilted at an angle $\theta_{tilt}=59.2^\circ$ relative to the optical axis direction [19].

In the tracker, sketched in Fig. 1 it is possible to identify three different regions. A drift region defined by the cathode and the Frish grid, a multiplication region which extends between the Frish grid and the proportional wires, and an induction region which extends between the DC wires and the segmented anode.

The drift region is defined by the cathode, an aluminum plate 1200×90 mm² large that is usually biased at voltage values ranging between -900 and -1500 V and a Frish grid, that is made of ten gold-plated tungsten wires with a diameter of $50 \mu\text{m}$ placed at a distance of 5 mm one from each other. In order to make as uniform as possible the electric field of the drift region

and to shield the inner electric field from the high voltage applied to the silicon detectors at the stopping wall [20], the active area of the tracker is surrounded by a double partition grid consisting of 41 couples of rings made of gold-plated wires.

The multiplication region is 20 mm high and is defined by the Frish grid and the plane where 10 proportional wires are located. Each of the proportional wires is 50 μm thick and is made of gold-plated tungsten. Such wires are biased to a voltage usually in the range between +500 V and +1300 V, provided by a common power supply. The ten wires are shared among the six proportional counters DC_i , $i=1, \dots, 6$. DC_2 and DC_5 have just a single wire while the other DCs have two proportional wires as shown in Fig. 2. An additional partition grid similar to the one used in the drift region is present with the aim to reduce the border effects of the electric field in the multiplication region.

The induction region is defined by the plane where the 10 proportional wires lay and the anode: the latter consisting of a segmented read-out plane. In Fig. 2 a bottom view of the anode is shown. The anode is divided in 6 longitudinal strips, one for each DC, being the strip corresponding to DC_2 and DC_5 8 mm wide while the others are 16 mm wide. Each strip is further segmented in pads (221 for DC_2 and DC_5 and 223 for $\text{DC}_{1,3,4,6}$) oriented along the spectrometer optical axis, that is with an angle equal to θ_{tilt} , see Fig. 2.

2.2. The silicon stopping wall

The silicon stopping wall is embedded in the gas filling the tracker to avoid further dead layers. The stopping wall is made of 57 silicon detectors arranged in 19 columns. Each detector is $50 \times 70 \text{ mm}^2$ wide and 500 μm or 1000 μm thick depending on the range of the ions to stop. They are mounted orthogonally to the optical axis of MAGNEX in order to minimize the effective dead layer. The closest distance of the silicon detector from the active area of the tracker is 15 mm that is enough to avoid interference with the electric field of the drift region of the tracker.

2.3. The working principle

When an incident particle crosses the entrance window entering the drift region, it generates a track of ions and electrons in the gas. The presence of a uniform electric field of about 50 V/cm in the drift region makes the ions drift towards the cathode and the electrons towards the Frish grid, these last with

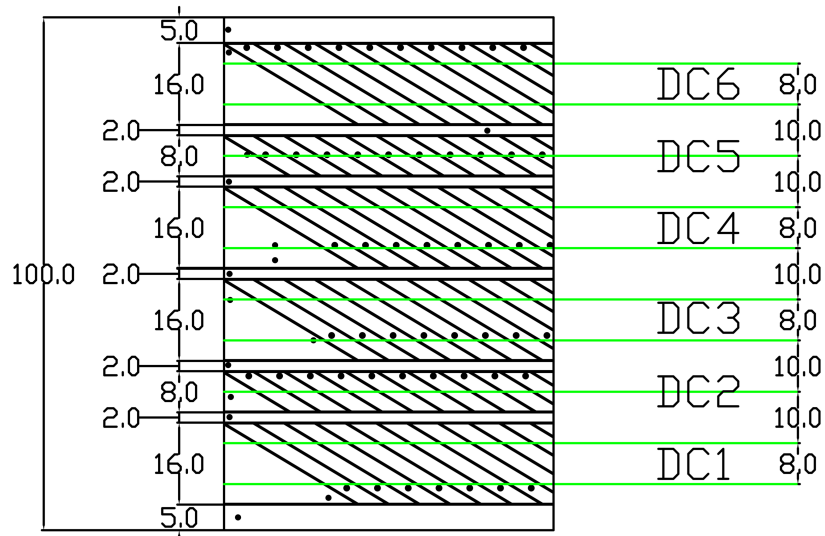


Figure 2: Scale drawing of a small portion of the segmented anode (bottom view). In the drawing the six strips of the anode that corresponds to the six drift chambers DCs are shown . Each strip is further segmented in pads that are tilted of $\theta_{ilt}=59.2^\circ$. In green the proportional wires are shown.

a velocity of about $5 \text{ cm}/\mu\text{s}$ [16]. After the Frish grid the primary electrons enter the multiplication region, are then accelerated by the strong electric field generated by the proportional wires and the multiplication occurs. Since the gas counters work in a proportional regime, the avalanches produced close to the wires generate a signal on the wires themselves which is proportional to the energy loss of the ion in the gas. Therefore six independent measurements of the energy loss are available, one for each DC.

In addition to the signal produced on the DC wires, the electron avalanche produced close to the wires induces a charge in a given number of pads of the strip laying just above the wires. The center of gravity of the charge distribution of the pads corresponding to a given DC is extracted. The six centers of gravity are converted in horizontal position providing six independent measurements X_i with $i = 1, \dots, 6$. From them, the position of the crossing point between the ion track and the focal plane X_f as well as the horizontal angle of the track θ_f is obtained. After crossing the gas tracker the ions hit the silicon detector stopping wall.

The vertical position is extracted by measuring the arrival time of the

electron avalanches in the wires taking advantage of the fact that the tracker works in a regime where the drift velocity is almost constant in the whole volume of the detector. Six vertical positions are extracted measuring the drift time of the primary electrons along in the drift region. The start signal is generated when the ion producing the track hits one of the silicon detector of the stopping wall. The six vertical positions Y_i with $i = 1, \dots, 6$ are used to obtain the vertical position Y_f on the focal plane detector and the angle ϕ_f of the ion track. The 57 silicon detectors of the stopping wall, in addition to the start signal for the drift time measurements, provide also the residual energy of the ions that is used mainly for identification purposes.

Thanks to the very small dead layer, almost entirely due to the mylar[®] window, the energy threshold for the detection of charged particles crossing the FPD is about 0.5 MeV/u.

3. Detector performances

The FPD was tested with a ^{18}O beam delivered by the tandem MP at INFN Laboratori Nazionali del Sud in Catania, Italy, at an energy of 84 MeV impinging on thin gold and carbon targets. The interaction between the beam particles and the target took place in the center of the MAGNEX scattering chamber. The angle between the optical axis of the spectrometer and the beam direction is named θ_{opt} . The spectrometer worked in full-acceptance mode which means an angular range $(\theta_{opt} - 5.2^\circ) < \theta_{lab} < (\theta_{opt} + 6.3^\circ)$ [21, 22]. Two collimators were installed upstream the target in order to limit the spot size and angular divergence of the beam at the target position to $1.78 \text{ mm} \times 1 \text{ mrad}$ in the horizontal direction and $2.8 \text{ mm} \times 1.2 \text{ mrad}$ in the vertical one. In some of the runs a multi-hole collimator was placed 206 mm downstream the target in order to select ejectiles with well defined trajectories. The multihole collimator has 65 circular holes with a diameter of 1 mm, arranged in five rows 11.5 mm spaced and 13 columns 3 mm spaced. The ions coming from the target which enter in the spectrometer acceptance were momentum analyzed and focused on the FPD. The FPD was filled with isobutane C_4H_{10} at a pressure of 15 mbar. In the following section we will analyze the main characteristics of the FPD, that is the resolution of the energy lost in the gas; the angular resolution; the position resolution, and the particle identification performances.

3.1. Energy loss measurements

Even if the energy loss measurement of the new FPD is based on the same principles as the old one Ref. [15], some difference is present. In fact the old FPD was composed of five drift chambers, but, usually, only the central one, the largest, was used to measure the energy loss ΔE . In the present FPD, there are six independent drift chambers with comparable active volume (DC₁, DC₂, DC₃, DC₄, DC₅, DC₆). The total active volume of the six drift chambers is larger than the volume of the single drift chamber used in the old FPD for the ΔE measurement. This fact ensures higher charge collection and therefore a better energy resolution for the new FPD, in the same ionization conditions.

Before making any further consideration on the ΔE measurements we have to underline that the FPD of a large-acceptance spectrometer should be designed to measure trajectories with very different incident angles θ_f and therefore with different effective lengths inside the FPD itself. In the case of MAGNEX the FPD is tilted of $\theta_{tilt}=59.2^\circ$ relative to the central trajectory, and θ_f (angle in the dispersive direction) ranges between a minimum value of 40° and a maximum value of 72° .

Therefore the linear length of the trajectory inside the active volume of the FPD can range from about -35% up to about +65% of the central trajectory. The contribution coming from the non-dispersive direction is almost negligible since the angle in ϕ ranges from -2° to $+2^\circ$ [12].

As a consequence the ΔE measurement is corrected for the effective thickness and normalized to the energy loss of the reference trajectory angle $\theta_{tilt}=59.2^\circ$. Therefore we introduce the quantity ΔE_{corr} :

$$\Delta E_{corr} = \Delta E \frac{\cos\theta_f}{\cos\theta_{tilt}} \quad (1)$$

To evaluate the effectiveness of this correction procedure the elastic scattering of ^{18}O beam at 84 MeV on a $122 \mu\text{g}/\text{cm}^2$ thick gold target was used. The FPD was working with 99.95%-pure isobutane gas at a pressure of 15 mbar. The voltage applied to the cathode and wires were -1000 V and +720 V respectively. The effect of such a correction is shown in Fig. 3. In the left panel ΔE as a function of θ_f is shown and it is evident the dependence of the measured energy loss from the horizontal incident angle θ_f . In right panel, where ΔE_{corr} as a function of θ_f is shown, the dependence of the energy on the angle θ_f is removed as expected. It is, therefore, evident that a

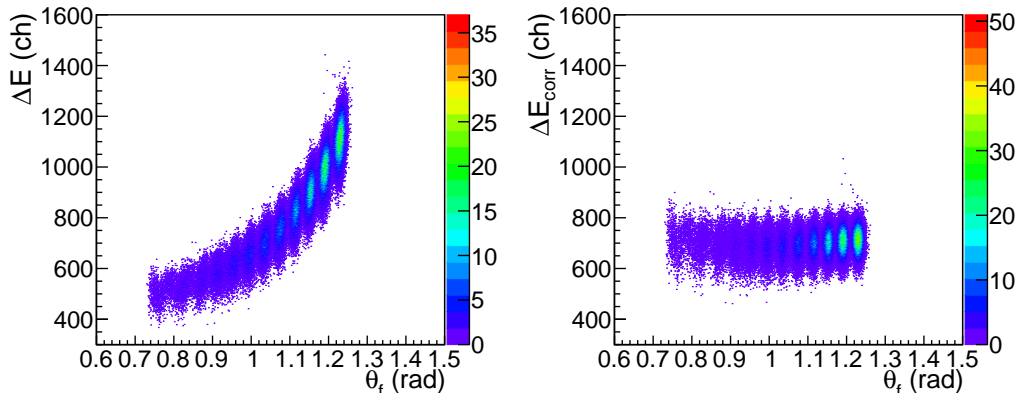


Figure 3: Left pad Energy loss (ΔE_{corr}) as a function of θ_f , right pad energy loss (ΔE_{corr} corrected for the effective path as a function of θ_f).

precise measurement of the angle θ_f is not only important for reconstruction purposes but it is also critical for identification purposes using the ΔE -E technique.

Border effects for the charge-collection efficiency are known to be present in particular at the entrance and exit of the FPD, where the electric field could be not uniform. Such non uniformity can worsen the tracking performances and generate a dependence of the collected charge from the y -coordinate. In order to mitigate such effects the voltage of the partition grid in the electron multiplication region was varied looking for the achievable best condition. The change of the energy channel for different values of the partition grid potential, all other parameters being equal, is shown in Fig. 4 where y vs ΔE_{corr} is plotted for DC_1 (example of a border DC) and DC_3 (example of a central DC). Different colors correspond to different bias applied to partition grid potential. For the case of the central DC_3 there is no effect, for DC_1 there is a strong effect that reduces the amplitude of the energy loss signals and virtually removes the dependence on the y coordinate.

In order to study the intrinsic resolution of the energy loss (ΔE) measurement, the elastic scattering data collected with the multiple hole collimator were analyzed. Moreover, the events corresponding to each hole of the collimator were selected with a condition in θ_f ($\Delta\theta_f < 2$ mrad) and y ($\Delta y < 2$ mm) in order to remove the dependence on the ion trajectory. While the FWHM of the ΔE_{corr} distribution for each single DC_i was about 10%, the

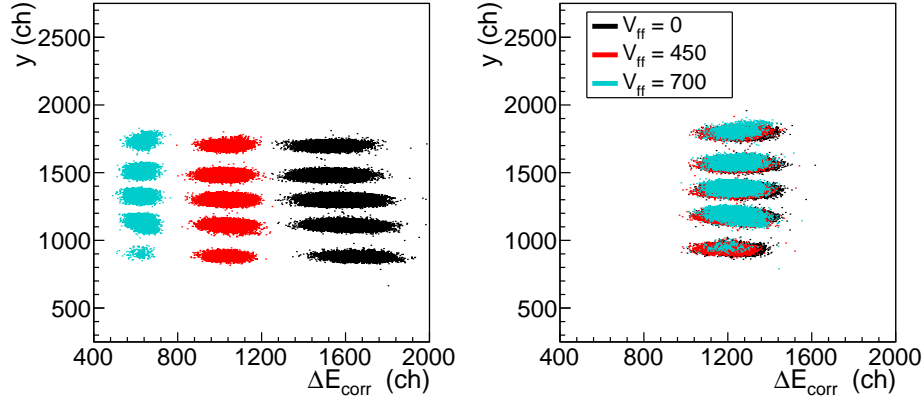


Figure 4: y-coordinate versus ΔE lost in the gas for DC₁ on the left and for DC₃ on the right. Each value of the voltage applied to the fringing field is represented as a different colour.

overall resolution obtained by summing all the energy measured by the six DCs is about 5%. The total energy here considered is given by

$$\Delta E_{tot} = \Delta E_{corr1} + \Delta E_{corr2} + \Delta E_{corr3} + \Delta E_{corr4} + \Delta E_{corr5} + \Delta E_{corr6}$$

The result does not depend significantly on the particular value of θ and y . An example of such calibrated energy spectrum is shown in Fig. 5.

3.2. Particle identification

In this section the particle identification procedure and typical results for the new MAGNEX FPD are shown. The data were taken using a ^{18}O beam at 84 MeV impinging on a $238 \mu\text{g}/\text{cm}^2$ thick ^{12}C target. The spectrometer was set at $\theta_{opt}=10^\circ$.

In Fig. 6 the energy lost in the drift chamber corrected for the incident angle (ΔE_{corr}) versus the residual energy E_{res} measured by one of the silicon detectors is shown. The different loci correspond to different values of the atomic number Z .

In Fig. 7 the position on the FPD X_f versus the residual energy E_{res} in one of the silicon detectors is shown. In this plot ions with the same Z gather on lines with the same slope, larger (smaller) slopes correspond to larger (smaller) Z . Ions having same Z but different masses can be identified as lines with the same slope but shifted at smaller (larger) X_f value for low (high)

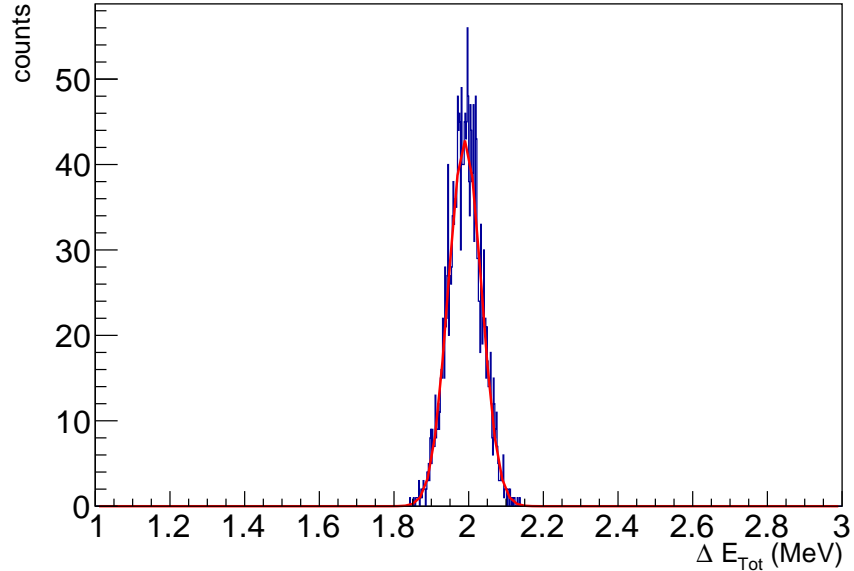


Figure 5: Example of distribution of the total energy lost in the six DCs using a multi-hole collimator. The FWHM extracted is about 5%. See text for more details.

masses. This is the result of the relationship between the kinetic energy (related to the parameter E_{res}) and the magnetic rigidity (related to the parameter X_f) of the charged particles traversing a magnetic spectrometer. This identification technique has been reported in details in Ref. [23]. These lines can be transformed in vertical lines using a rotation in the plane $X_f - E_{res}$ as shown in Fig 8. After the rotation, the loci corresponding to oxygen isotopes with charge state 8^+ are selected, thus a cut on X_f is performed and, eventually, they are projected on the x-axis (Fig. 9). From this figure the mass resolving power of the FPD can be determined; it is defined as $R = M/\Delta M$, where M is the mass of the central peak and ΔM is the FWHM of such peak. For example for oxygen ions the resolving power, in this specific working conditions, is $M=1/136$, as shown in Fig. 9.

3.3. Position and angle measurements in the dispersive direction

The position along the horizontal direction is determined by means of the distribution of charge induced on the pads. The number of hit pads is usually between 5 and 25 depending mainly on the incident angle of the ion θ_f and its energy loss. A generalization of the center of gravity method [24]

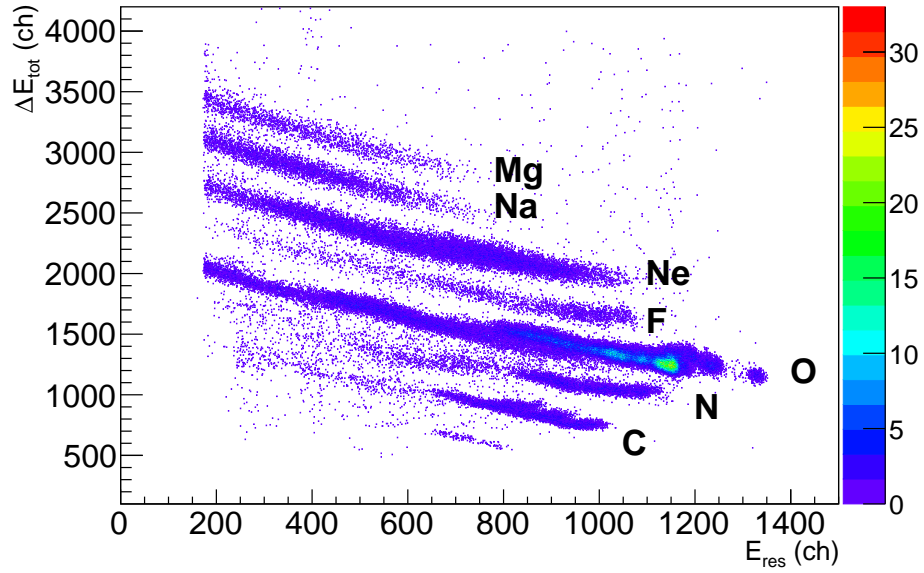


Figure 6: Typical $\Delta E_{tot} - E_{res}$ plot for single silicon detector. Loci of isotopes from carbon to magnesium are well separated.

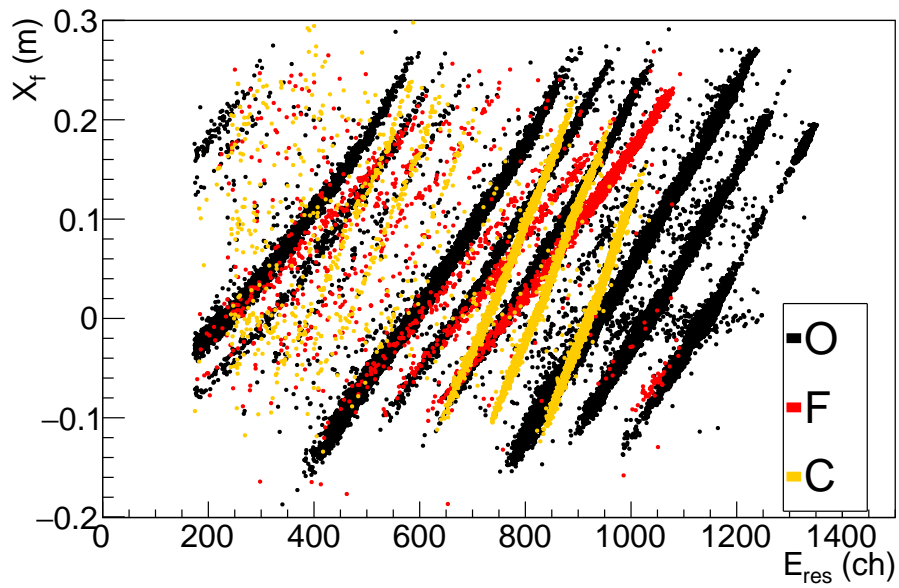


Figure 7: Typical X_f vs E_{res} plot for a single silicon detector.

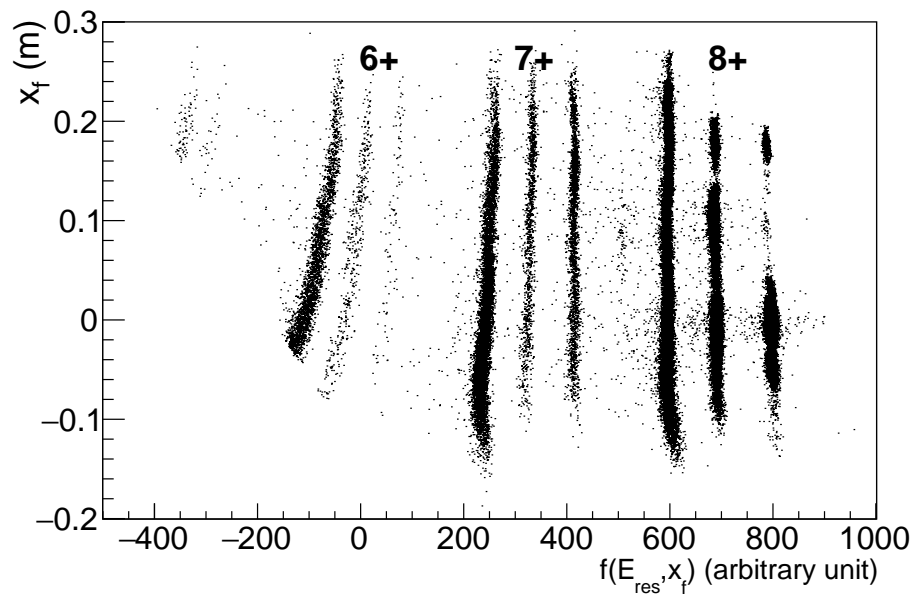


Figure 8: X_f vs a function of the residual energy and the position on the focal plane $f(E_{res}, x_f) = E_{res} - (a \times x_f^2 + b \times x_f + c)$ for oxygen ions. It is possible to identify ions with different charge states: 6^+ , 7^+ , 8^+ .

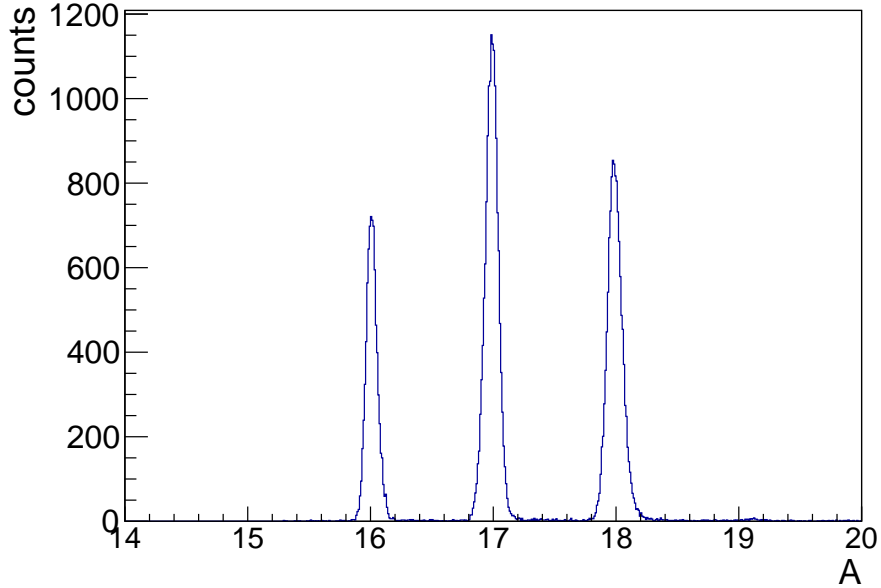


Figure 9: Mass distribution extracted from Fig. 8 for the oxygen ions: $A=16, 17, 18$ with a 8^+ charge state.

is used to extract the centroid of the charge distribution as discussed in Refs. [25, 15].

The position resolution has been estimated using the multi-hole collimator. Several effects can influence the estimate of the position resolution like: the size of the collimator holes, the beam-spot size, multiple scattering in the detector itself, and straggling in the entrance window. These effects can be partially compensated by considering the difference between two coordinates as, for example, $X_i - X_3$ instead that a single coordinate X_i . X_3 was chosen as reference wire since, being a central drift chamber, it is less sensible to border effects that could affect the edge drift chambers.

In Fig. 10 the angle θ_f versus $X_3 - X_4$ is shown after a gate on the elastic scattering was applied. Each spot of the plot corresponds to a bunch of trajectories passing through the same hole having a given average angle θ_f at the focal plane. As θ_f increases the $X_3 - X_4$ distribution of each spot becomes broader.

For each spot of Fig. 10 a narrow gate of 2 mrad in θ_f was applied and the position distributions of all the X_i variables were obtained. Such angular

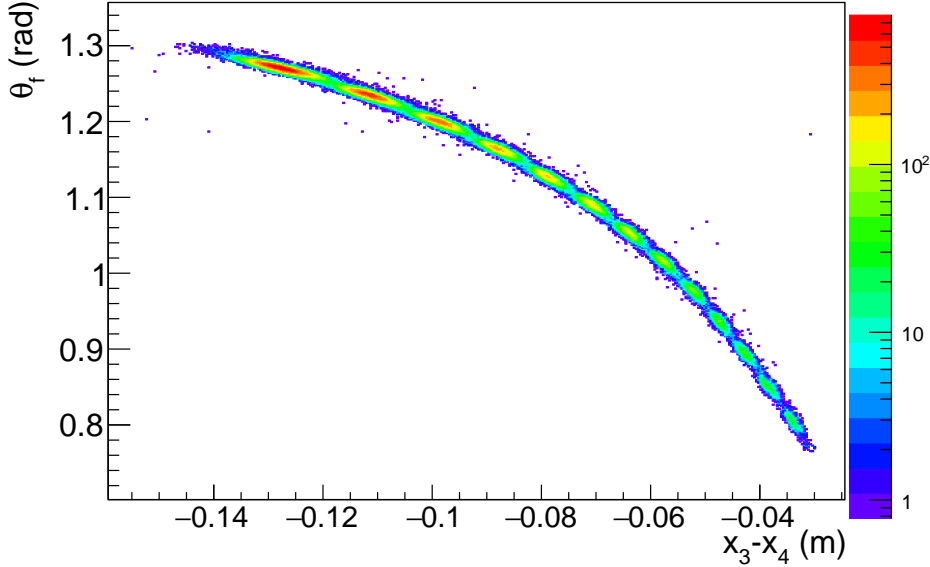


Figure 10: θ_f angle versus the $\Delta x = X_3 - X_4$.

spread corresponds, for example, to a position spread of about 0.12 mm at $\theta = 40^\circ$ and 0.65 mm at $\theta = 72^\circ$. This geometrical contribution to the overall width of the position distribution is shown in Fig. 11 as a continuous line for all the X_i , while points correspond to the experimental FWHM measured at each angle. The horizontal resolution $X_i - X_3$ was estimated for all the wires. No significant difference between different DC_i was found. The final resolution is estimated to be around 0.6 mm for each wire.

All the coordinates X_i , $i = 1, \dots, 6$ are used, together with the longitudinal coordinates Z_i , $i = 1, \dots, 6$ for the definition of the horizontal angle θ_f . The use of six points guarantees a better precision compared to the previous FPD that used just four points.

The plot of measured θ_f is shown in Fig. 12. Each peak in the plot corresponds to trajectories passing through one of middle-row hole of the multi-hole collimator. The difference in counts for each peak is due to different cross section of the elastic scattering at different angles.

The method used to estimate the angular resolution is described in detail in the following. The first step consists in selecting a group of trajectories by applying a gate on the first and the last DCs, (i.e. DC_1 and DC_6). The

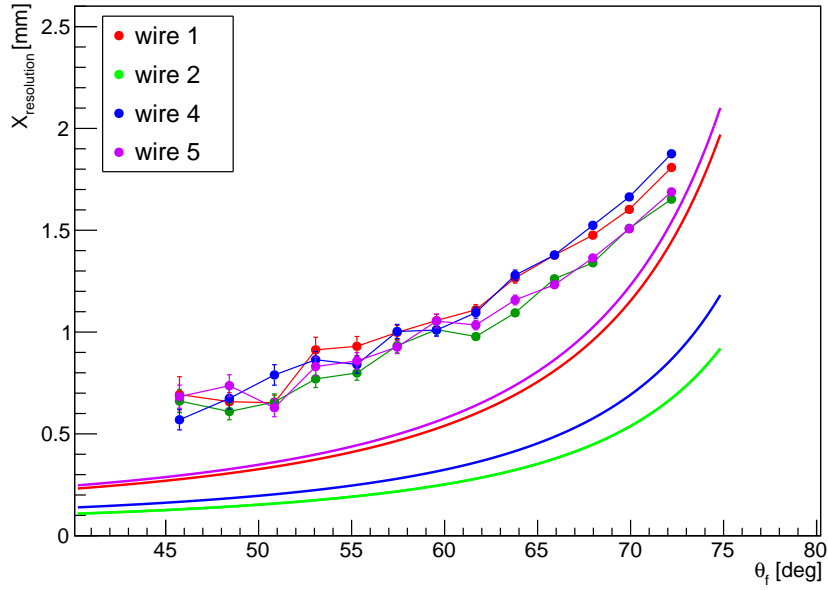


Figure 11: Horizontal resolution (FWHM) as a function of the angle θ_f . The lines represent the geometrical contribution to the resolution due to the selected angle.

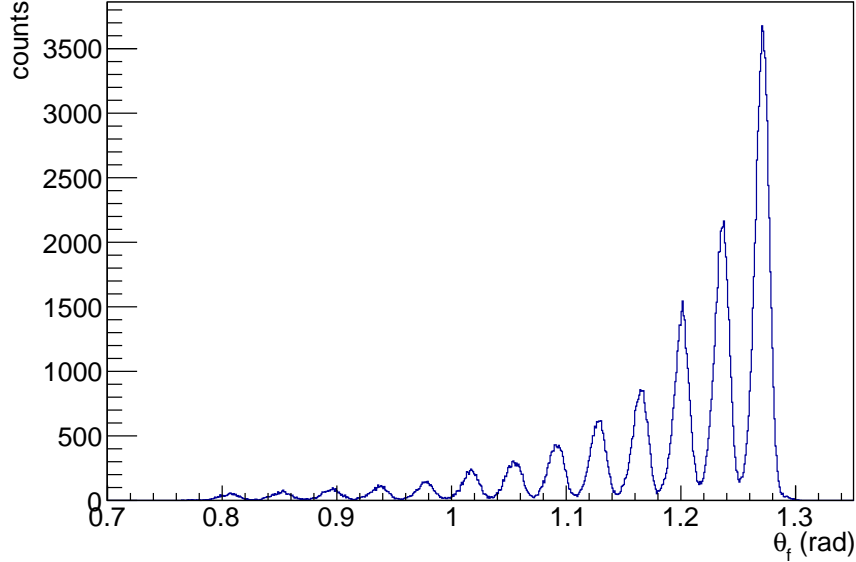


Figure 12: Plot of the θ_f angle after a selection in the elastically scattered ^{18}O ions and in the trajectories passing through the middle-row holes of the multi-hole collimator.

trajectories are selected with an average θ_f value of 1000 mrad and a FWHM of 3.2 mrad.

In the second step the trajectory of the events selected in the first step are extracted, using the X_i obtain from the other four DCs, thus excluding X_1 and X_6 . The angular distribution of such events has a spread of 3.9 mrad (FWHM), taking into account the initial spread of selected trajectories it is possible to extract a value for the θ_f resolution of the tracker of 2.2 mrad (FWHM). The resolution here extracted should be considered as an upper limit of the actual θ_f resolution, since the resolution of the full tracker is done using six X-positions for each events instead of the previous four X-positions we were using for the θ_f resolution estimation. The resolution here obtained is much better than the previous detector, where 5 mrad (FWHM) was obtained using a similar procedure.

3.3.1. The cross-talk effect

A phenomenon present in the old FPD that affected the horizontal position measurements of the ion track is the cross-talk [25]. In fact, the electron avalanche produced by a given proportional wire can induce a charge also

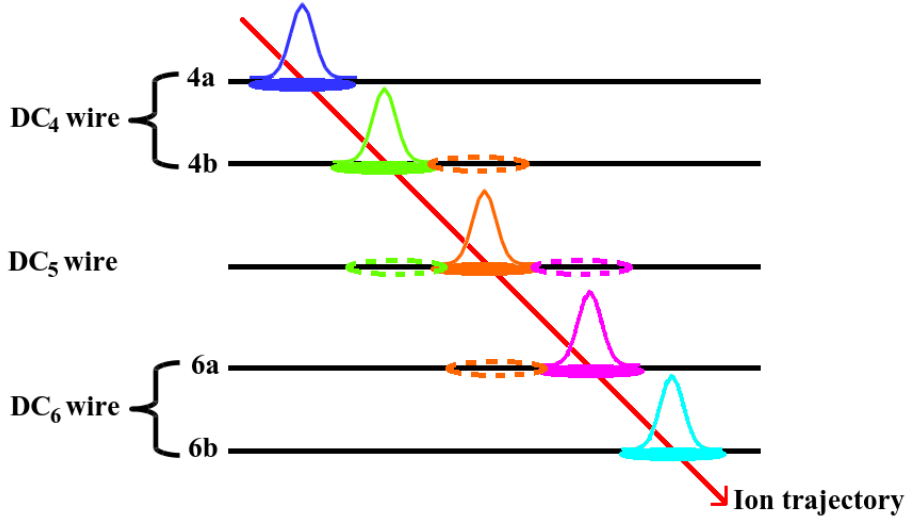


Figure 13: Schematic representation of the induction signal formation in the regions of DC₄, DC₅ and DC₆ multiplication wires. The areas of the main charge induction are denoted with the filled contours, while the areas denoted with the dotted contours correspond to the cross-talk induced signal.

in pads corresponding to a neighboring wire. Therefore, the resulted charge distributions measured for a given wire may be distorted affecting the final determination of the X_i coordinate.

In order to mitigate this problem some modification in the new FPD design was required. The geometry of the wires and strips was changed making the average distance between two adjacent strips larger than the distance between each wire and the corresponding strip. The segmented strips were separated from each other by a 2 mm spacer as shown in Fig. 2.

We briefly describe the adopted procedure for estimating the cross-talk induced signal on DC₅ strip for a typical event, the same procedure can be extended for the other DCs. As a first step, the measured induced charge distributions of DC₄ and DC₆ wires were fitted each by a Gaussian function. Since DC₄ and DC₆ are composed by two wires each (see Fig. 2) the charge distribution was decomposed into two internal Gaussian curves, each one describing the induced charge of each wire. Then, having determined the height A , the centroid (mean value) and the standard deviation σ of the distributions, each one was further decomposed into two Gaussian functions

with:

$$A_a = A_b \approx A/2 \quad (2)$$

$$\sigma_a = \sigma_b \approx \sigma \quad (3)$$

where, A_a , A_b are the heights and σ_a , σ_b are the standard deviations of the two Gaussian functions. These so called "internal" Gaussian functions are associated to the signal originating the induced charge of each of the two wires composing DC₄ and DC₆, namely, DC_{4a}, DC_{4b}, DC_{6a} and DC_{6b}. In the last step of the analysis, the DC_{4b} and DC_{6a} distributions were superimposed to the measured induced signal of DC₅ and were renormalized such as to describe the shape of the distribution. The results of the charge distribution analysis for DC₅ for a single elastic scattering event with $\theta_f \approx 62^\circ$ are presented in Fig. 14. It is evident that the distortion in the shape of the charge distribution caused by the cross-talk is small. In addition, the amplitude of cross-talk signal is well-below the level of the threshold, which was determined through an iterative procedure by means of the optimized Center Of Gravity (COG) algorithm [25]. Therefore, we may conclude that the cross-talk phenomena are under control.

3.4. Vertical position and angle measurements

The Y resolution has been calculated plotting Y_3 versus the difference $Y_1 - Y_2$ shown in Fig. 15. The five spots correspond to the particle passing through each of the five vertical rows of holes of the multi-hole collimator. The FWHM of each spot on the abscissa-projection is 0.6 mm giving a resolution of about 0.4 mm for the single CD.

The vertical angle ϕ is obtained by a linear fit of the six vertical positions $Y_1, Y_2, Y_3, Y_4, Y_5, Y_6$ and the six coordinates $Z_1, Z_2, Z_3, Z_4, Z_5, Z_6$ defined by the position of the six drift chambers. That is

$$Z_i = a_0 + a_1 Y_i \quad (4)$$

where a_1 is $\tan(\phi)$. For the estimate of the angular resolution we used the formula for the error of the parameters of a linear fit:

$$\sigma_{a_1}^2 = \sum_{i=1}^N \left(\frac{\partial a_1}{\partial y_i} \sigma_y \right)^2 = \sigma_y^2 \frac{N}{N (\sum_{i=1}^N y_i^2) - (\sum_{i=1}^N y_i)^2} \quad (5)$$

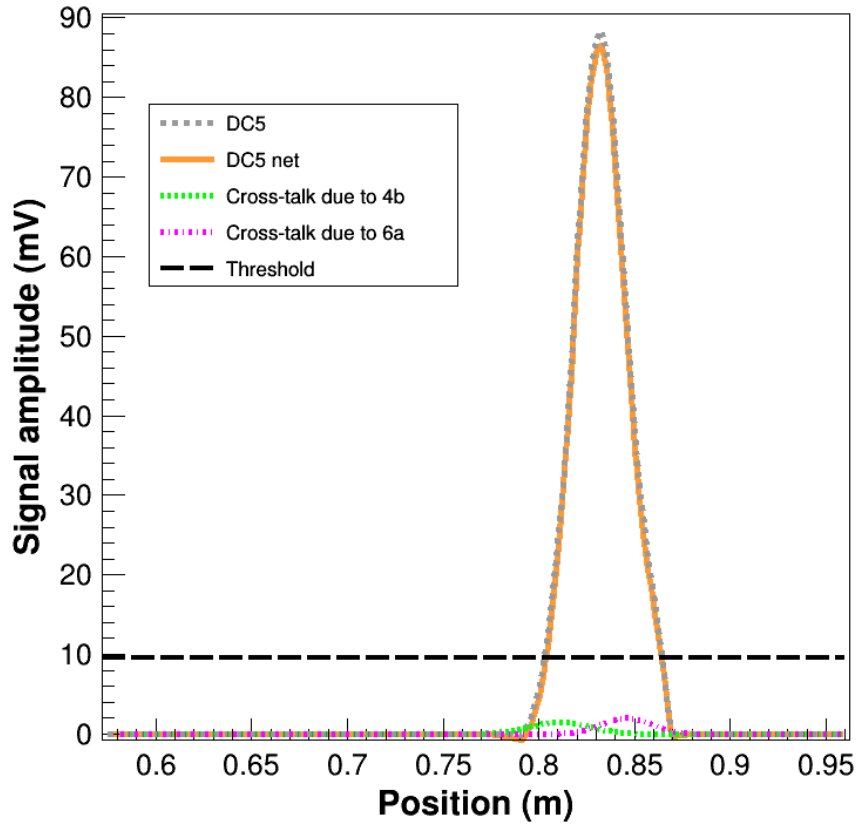


Figure 14: Charge distribution analysis for the induction pads over the DC₅ proportional wire. The dashed gray line corresponds to the total charge distribution collected by the induction pads over the DC₅ wire. The dashed green and the dashed-dotted magenta lines represent the cross-talk induced signal from DC_{4b} and DC_{6a} wires respectively. The solid orange line corresponds to the signal after subtracting the cross-talk contribution and the dashed black line represents the value of the threshold as it was determined using the COG algorithm [25].

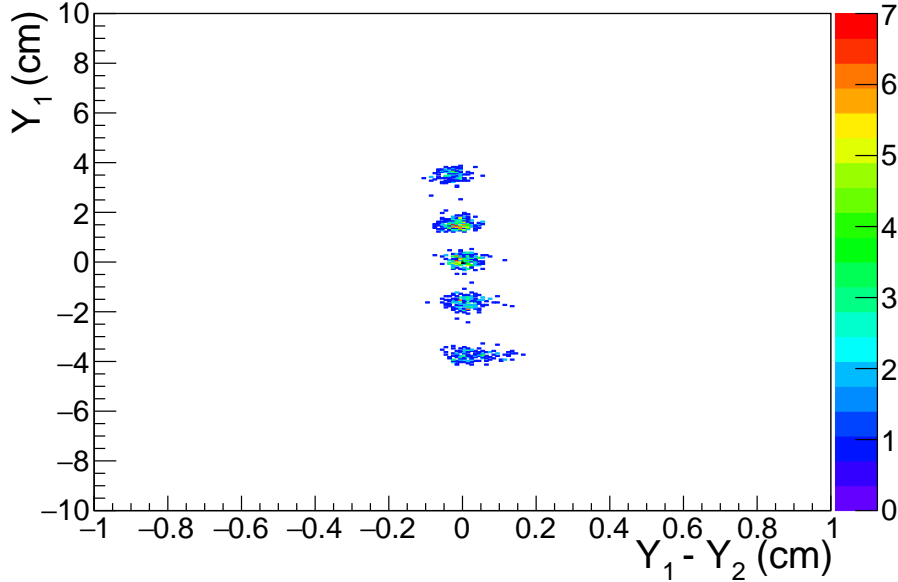


Figure 15: y-coordinate versus the $Y_1 - Y_2$.

where in place of $N (\sum_{i=1}^N y_i^2) - (\sum_{i=1}^N y_i)^2$ the Y resolution have been used. The resolution $\delta\phi$ depends on the horizontal angle of the particle trajectory θ_f since this influences the actual trajectory length inside the tracker. It ranges from 0.3 to 0.7 mrad for trajectories with $\theta_f=40^\circ$ and $\theta_f=70^\circ$ respectively. We conclude that, also in the vertical direction the position resolution as well the angular resolution are better than those of the previous detector.

4. Summary and Conclusions

The new focal plane detector of the large-acceptance MAGNEX spectrometer has been described underlining the innovative aspects relative to the previous FPD.

It keeps many characteristics of the old FPD, that is the capability to work at pressure ranging from few mbar to several tenth of mbar using a thin entrance window. This guarantees a very low detection threshold and the capability to identify particles in a broad range of ionizing condition. The main characteristics of the new MAGNEX focal plane detector and position and angular resolution obtained by using the scattering of ^{18}O beam of 84 MeV are listed in Tab. 4.

Table 1: Main characteristics of the new FPD of MAGNEX spectrometer.

Energy loss resolution for ^{18}O	5%
Horizontal position resolution	0.6 mm
Horizontal angular resolution	2.2 mrad
Vertical position resolution	0.4 mm
Vertical angular resolution	0.5 mrad

The new design based on the segmentation of the gas tracker in six drift chambers all of similar size guarantees better performances in terms of tracking precision. The track is now sampled in six positions to be compared to the four of the old FPD, with a consequent better position and angular resolution of the ion tracks. The energy loss the performances have been improved since a longer portion of the track in the ionizing gas is sampled compared to the previous FPD, guaranteeing an higher resolution and therefore a better identification capability. In the design of the new detector, a special care has been given to reduce the effects of the cross-talk between neighboring strips. In the new FPD the cross-talk has been minimized and its effects on the track reconstruction are now negligible.

Acknowledgments

This project has received funding from the European Union’s Horizon 2020 research and innovation program under the ERC grant agreement GA 714625.

References

- [1] K. Kisamori, S. Shimoura, H. Miya, S. Michimasa, S. Ota, M. Assie, H. Baba, T. Baba, D. Beaumel, M. Dozono, T. Fujii, N. Fukuda, S. Go, F. Hammache, E. Ideguchi, N. Inabe, M. Itoh, D. Kameda, S. Kawase, T. Kawabata, M. Kobayashi, Y. Kondo, T. Kubo, Y. Kubota, M. Kurata-Nishimura, C. S. Lee, Y. Maeda, H. Matsubara, K. Miki, T. Nishi, S. Noji, S. Sakaguchi, H. Sakai, Y. Sasamoto, M. Sasano, H. Sato, Y. Shimizu, A. Stolz, H. Suzuki, M. Takaki, H. Takeda, S. Takeuchi, A. Tamii, L. Tang, H. Tokieda, M. Tsumura, T. Uesaka, K. Yako, Y. Yanagisawa, R. Yokoyama, K. Yoshida, Candidate resonant

tetraneutron state populated by the $^4\text{He}(^8\text{He},^8\text{Be})$ reaction, *Phys. Rev. Lett.* 116 (2016) 052501.

- [2] Cappuzzello, F., Agodi, C., Cavallaro, M., Carbone, D., Tudisco, S., Lo Presti, D., Oliveira, J. R. B., Finocchiaro, P., Colonna, M., Rifuggiato, D., Calabretta, L., Calvo, D., Pandola, L., Acosta, L., Auerbach, N., Bellone, J., Bijker, R., Bonanno, D., Bongiovanni, D., Borello-Lewin, T., Boztosun, I., Brunasso, O., Burrello, S., Calabrese, S., Calanna, A., Chávez Lomelí, E. R., D'Agostino, G., De Faria, P. N., De Geronimo, G., Delaunay, F., Deshmukh, N., Ferreira, J. L., Fisichella, M., Foti, A., Gallo, G., Garcia-Tecocoatzi, H., Greco, V., Hacisalihoglu, A., Iazzi, F., Introzzi, R., Lanzalone, G., Lay, J. A., La Via, F., Lenske, H., Linares, R., Litrico, G., Longhitano, F., Lubian, J., Medina, N. H., Mendes, D. R., Morales, M., Muoio, A., Pakou, A., Petrascu, H., Pinna, F., Reito, S., Russo, A. D., Russo, G., Santagati, G., Santopinto, E., Santos, R. B. B., Sgouros, O., da Silveira, M. A. G., Solakci, S. O., Souliotis, G., Soukeras, V., Spatafora, A., Torresi, D., Magana Vsevolodovna, R., Yildirim, A., Zagatto, V. A. B., The numen project: Nuclear matrix elements for neutrinoless double beta decay, *Eur. Phys. J. A* 54 (5) (2018) 72.
- [3] D. Pereira, R. Linares, J. Oliveira, J. Lubian, L. Chamon, P. Gomes, A. Cunsolo, F. Cappuzzello, M. Cavallaro, D. Carbone, A. Foti, Nuclear rainbow in the $^{16}\text{O}+^{27}\text{Al}$ system: The role of couplings at energies far above the barrier, *Physics Letters B* 710 (3) (2012) 426 – 429. doi:<https://doi.org/10.1016/j.physletb.2012.03.032>. URL <http://www.sciencedirect.com/science/article/pii/S0370269312003061>
- [4] T. Kobayashi, N. Chiga, T. Isobe, Y. Kondo, T. Kubo, K. Kusaka, T. Motobayashi, T. Nakamura, J. Ohnishi, H. Okuno, H. Otsu, T. Sako, H. Sato, Y. Shimizu, K. Sekiguchi, K. Takahashi, R. Tanaka, K. Yoneda, Samurai spectrometer for ri beam experiments, *Nuclear Instruments and Methods in Physics Research Section B: Beam Interactions with Materials and Atoms* 317 (2013) 294 – 304, xVIth International Conference on ElectroMagnetic Isotope Separators and Techniques Related to their Applications, December 2–7, 2012 at Matsue, Japan.
- [5] T. Uesaka, S. Shimoura, H. Sakai, G. Berg, K. Nakanishi, Y. Sasamoto,

- A. Saito, S. Michimasa, T. Kawabata, T. Kubo, The high resolution sharaq spectrometer, *Nuclear Instruments and Methods in Physics Research Section B: Beam Interactions with Materials and Atoms* 266 (19) (2008) 4218 – 4222, proceedings of the XVth International Conference on Electromagnetic Isotope Separators and Techniques Related to their Applications.
- [6] A. Stefanini, L. Corradi, G. Maron, A. Pisent, M. Trotta, A. Vinodkumar, S. Beghini, G. Montagnoli, F. Scarlassara, G. Segato, A. D. Rosa, G. Inghima, D. Pierroutsakou, M. Romoli, M. Sandoli, G. Pollarolo, A. Latina, The heavy-ion magnetic spectrometer prisma, *Nuclear Physics A* 701 (1) (2002) 217 – 221, 5th International Conference on Radioactive Nuclear Beams.
- [7] M. Rejmund, B. Lecornu, A. Navin, C. Schmitt, S. Damoy, O. Delaune, J. Enguerrand, G. Fremont, P. Gangnant, L. Gaudefroy, B. Jacquot, J. Pancin, S. Pullanhiotan, C. Spitaels, Performance of the improved larger acceptance spectrometer: Vamos++, *Nuclear Instruments and Methods in Physics Research Section A: Accelerators, Spectrometers, Detectors and Associated Equipment* 646 (1) (2011) 184 – 191.
- [8] Cappuzzello, F., Agodi, C., Carbone, D., Cavallaro, M., The magnex spectrometer: Results and perspectives, *Eur. Phys. J. A* 52 (6) (2016) 167.
- [9] M. Cavallaro, C. Agodi, G. Brischetto, S. Calabrese, F. Cappuzzello, D. Carbone, I. Ciraldo, A. Pakou, O. Sgouros, V. Soukeras, G. Souliotis, A. Spatafora, D. Torresi, The magnex magnetic spectrometer for double charge exchange reactions, *Nuclear Instruments and Methods in Physics Research Section B: Beam Interactions with Materials and Atoms* 463 (2020) 334 – 338.
- [10] Oxford Handbook of Innovation, Nova Publisher Inc., New York, 2011, Ch. MAGNEX: an innovative large acceptance spectrometer for nuclear reaction studies.
- [11] A. Lazzaro, et al., *Inst. Phys. Conf. Ser.* 175 (2005) 171.
- [12] F. Cappuzzello, D. Carbone, M. Cavallaro, Measuring the ions momentum vector with a large acceptance magnetic spectrometer, *Nuclear Instruments and Methods in Physics Research Section A: Accelerators,*

- Spectrometers, Detectors and Associated Equipment 638 (1) (2011) 74 – 82.
- [13] S. Pullanhiotan, M. Rejmund, A. Navin, W. Mittig, S. Bhattacharyya, Performance of vamos for reactions near the coulomb barrier, Nuclear Instruments and Methods in Physics Research Section A: Accelerators, Spectrometers, Detectors and Associated Equipment 593 (3) (2008) 343 – 352.
- [14] Montanari, D., Farnea, E., Leoni, S., Pollarolo, G., Corradi, L., Benzoni, G., Gadea, A., Fioretto, E., Latina, A., Montagnoli, G., Scarlassara, F., Stefanini, A.M., Szilner, S., Response function of the magnetic spectrometer prisma, Eur. Phys. J. A 47 (1) (2011) 4.
- [15] M. Cavallaro, F. Cappuzzello, D. Carbone, A. Cunsolo, A. Foti, A. Khouaja, M. R. D. Rodrigues, J. S. Winfield, M. Bondi, The low-pressure focal plane detector of the magnex spectrometer, The European Physical Journal A 48 (5) (2012) 59.
- [16] B. Schmidt, Drift properties of electrons in methane and methane noble gas mixtures, Nuclear Instruments and Methods in Physics Research Section A: Accelerators, Spectrometers, Detectors and Associated Equipment 252 (2) (1986) 579 – 585.
- [17] A. Sharma, Muon tracking and triggering with gaseous detectors and some applications, Nuclear Instruments and Methods in Physics Research Section A: Accelerators, Spectrometers, Detectors and Associated Equipment 666 (2012) 98 – 129, advanced Instrumentation.
- [18] W. R. Leo, Techniques for Nuclear and Particle Physics Experiments, 2nd Edition, Springer-Verlag, 1994, Ch. 6, p. 150.
- [19] A. Cunsolo, F. Cappuzzello, A. Foti, A. Lazzaro, A. Melita, C. Nociforo, V. Shchepunov, J. Winfield, Ion optics for large-acceptance magnetic spectrometers: application to the magnex spectrometer, Nuclear Instruments and Methods in Physics Research Section A: Accelerators, Spectrometers, Detectors and Associated Equipment 484 (1) (2002) 56 – 83.

- [20] M. Cavallaro, First application of the magnex spectrometer: investigation of the $^{19}\text{f}(^7\text{li},^7\text{be})^{19}\text{o}$ reaction at 52.2 mev, Ph.D. thesis, Dipartimento di Fisica e Astronomia, Università di Catania (2008).
- [21] M. Cavallaro, F. Cappuzzello, D. Carbone, A. Cunsolo, A. Foti, R. Linares, D. Pereira, J. Oliveira, P. Gomes, J. Lubian, R. Chen, Challenging measurement of the $^{16}\text{o}+^{27}\text{al}$ elastic and inelastic angular distributions up to large angles, Nuclear Instruments and Methods in Physics Research Section A: Accelerators, Spectrometers, Detectors and Associated Equipment 648 (1) (2011) 46 – 51.
- [22] M. Cavallaro, F. Cappuzzello, D. Carbone, A. Cunsolo, A. Foti, R. Linares, Transport efficiency in large acceptance spectrometers, Nuclear Instruments and Methods in Physics Research Section A: Accelerators, Spectrometers, Detectors and Associated Equipment 637 (1) (2011) 77 – 87.
- [23] F. Cappuzzello, M. Cavallaro, A. Cunsolo, A. Foti, D. Carbone, S. Origo, M. Rodrigues, A particle identification technique for large acceptance spectrometers, Nuclear Instruments and Methods in Physics Research Section A: Accelerators, Spectrometers, Detectors and Associated Equipment 621 (1) (2010) 419 – 423.
- [24] G. Charpak, G. Melchart, G. Petersen, F. Sauli, High-accuracy localization of minimum ionizing particles using the cathode-induced charge centre-of-gravity read-out, Nuclear Instruments and Methods 167 (3) (1979) 455 – 464.
- [25] Carbone, D., Cappuzzello, F., Cavallaro, M., Universal algorithm for the analysis of charge distributions in segmented electrodes of gas detectors, Eur. Phys. J. A 48 (5) (2012) 60.